RESEARCH ARTICLE

NANO · MICRO small
www.small-journal.com

Dual-Functional Phosphorus-Doped Iron Single-Atom Catalyst on Reduced Graphene Oxide for Efficient Lithium–Sulfur Batteries: Simultaneous Polysulfides Trapping/Catalysis and Lithium Deposition Regulation

Abdul Hameed Pato, Longtao Ren, Imran Ali Chandio, Qiaoli Zhang, Yizhe Li, Jinrui Liang, Mengchao Li, Safdar Abbas, Elhussein Desoki Helal, and Wen Liu**

The development of high-performance lithium–sulfur (Li–S) batteries is hindered by the complex interplay of lithium polysulfides (LiPSs) shuttle effects and uncontrolled lithium dendrite growth. Herein, we introduce a dual-functional—phosphorus-doped iron single-atom catalysts on reduced graphene oxide (Fe-NPC@rGO)—to address both issues. Density functional theory (DFT) and experiments reveal that Fe-NPC@rGO enhances sulfur redox kinetics and regulates lithium deposition. The Fe–NPC high charge density and enhanced electron transfer (vs. Fe–N4) enable Fe–NPC@rGO to trap polysulfides (LiPSs) and boost their conversion, reducing shuttle effects. Simultaneously, its lithiophilic properties enable uniform Li plating, inhibiting dendrites. Li–S cells with Fe–NPC@GO modified separators deliver a high discharge capacity of 1156 mAh g−1 at 1 C, with an exceptionally low-capacity decay of 0.032% per cycle over 1000 cycles. Moreover, full Li–S battery configuration (Fe−NPC@rGO-Li||Fe−NPC@rGO-PP||ROCNT-S) achieves high areal capacity of 4.9 mAh cm−2 at 5 mg cm−2 sulfur loading, low electrolyte to sulfur (E/S) ratio of 6 µL mg−1, and an ultralow negative to positive (N/P) ratio of 1.2. These findings provide valuable insights into the structural optimization of electrocatalysts and underscore the significant potential of Fe–NPC@rGO in advancing the electrochemical performance of next-generation Li–S batteries.

1. Introduction

The lithium–sulfur (Li–S) battery system is widely considered as one of the most promising candidates for next-generation energy storage technologies, owing to its high theoretical specific capacities (1675 mAh g^{-1} for sulfur and 3860 mAh g^{-1} for lithium), low mass densities (2.07 g cm^{-3} for sulfur and 0.534 g cm^{-3} for lithium), and environmental compatibility.[1–3] However, despite these advantages, the commercialization of Li–S batteries is severely hindered by a range of technical challenges associated with both the sulfur cathode and the lithium metal anode.[4–6] On the cathode side, the insulating nature of elemental sulfur and lithium sulfide (Li_2S), the shuttle effect of long-chain lithium polysulfides (LiPSs, Li_2S_n, $4 \leq n \leq 8$), and substantial volume expansion lead to sluggish reaction kinetics, low sulfur utilization, and a shortened cycle life.[7–9] At the same time, the lithium metal anode suffers from uncontrolled dendrite growth and infinite volume expansion, which pose significant safety concerns and result in low Coulombic efficiency (CE).[10–12] These challenges underscore the urgent need for innovative design strategies that address both the cathode and anode to enable the development of more sustainable, efficient, and stable Li–S batteries.[13–15]

Significant research has focused on addressing Li–S battery challenges through innovative cathode and anode engineering. For the cathode, strategies include sulfur encapsulation,[16–18] separator modification,[19,20] binder optimization,[21] and electrolyte enhancements.[22] Separator modification with polar materials (e.g., metals, metal compounds, and heteroatom-doped carbon) has been particularly effective in anchoring polysulfides chemically while maintaining ionic conductivity.[23,24] However, excessive inactive materials often reduce energy density limiting the overall performance of the batteries, compared to theoretical values. On the anode side, key approaches involve lithiophilic hosts,[25] electrolyte additives,[26,27] and artificial SEI layers.[28] Carbon nanostructures integrated with lithiophilic catalysts (e.g., transition metals) show promise for uniform lithium deposition but often suffer from high mass density, poor conductivity, and insufficient nucleation sites.[29–31] Additionally, conventional Li-S

A. H. Pato, L. Ren, I. A. Chandio, Q. Zhang, Y. Li, J. Liang, M. Li, S. Abbas, W. Liu
College of Chemistry
State Key Laboratory of Chemical Resource Engineering
Beijing University of Chemical Technology
Beijing 100029, China
E-mail: longtao.ren@buct.edu.cn; wenliu@mail.buct.edu.cn
E. D. Helal
Chemistry Department
Faculty of Science
Benha University
Benha 13518, Egypt

The ORCID identification number(s) for the author(s) of this article can be found under https://doi.org/10.1002/smll.202503596

DOI: 10.1002/smll.202503596

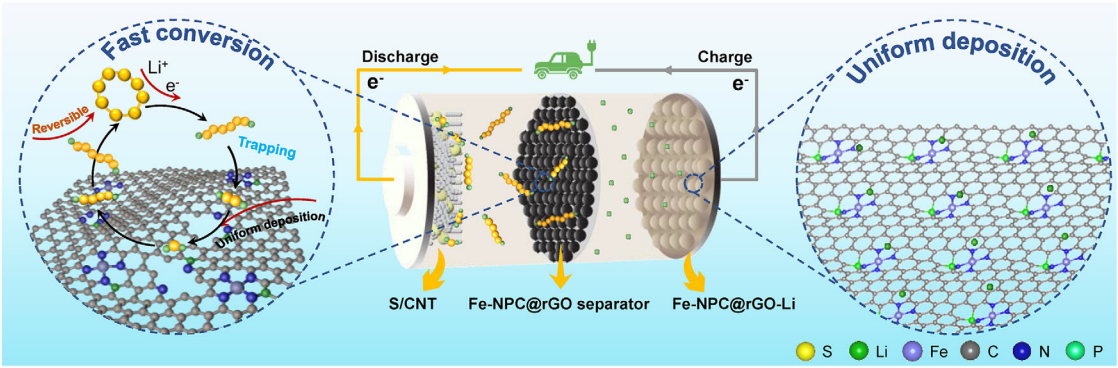

Scheme 1. Dual-functional Fe–NPC@rGO electrocatalyst showing fast LiPSs conversion and uniform lithium deposition in advanced Li–S batteries.

batteries use excess lithium, lowering energy density and masking true cycling performance.[13,32] These challenges underscore the need for integrated solutions that simultaneously optimize both electrodes while meeting commercial energy density requirements. Recent advances in multifunctional interlayers, hybrid electrolytes, and integrated electrode designs offer promising pathways to overcome these limitations and advance Li–S battery development.

A transformative approach involves dual-functional single-atom catalysts (SACs), which offer maximum atom utilization efficiency, well-defined coordination environments, and uniformly dispersed active sites, making them ideally suited to overcome the persistent limitations of Li–S systems.[33–36] While most SACs to date have focused on traditional M–N_4 configurations, these often exhibit limited LiPSs adsorption capacity and fail to ensure uniform lithium deposition, which limits their overall effectiveness. Recent advances suggest that asymmetrically coordinated SACs, which feature irregular geometric structures and electronic redistribution, could significantly improve catalytic performance by enhancing the adsorption and conversion of reaction intermediates.[37–39] This highlight the urgent need for dual-functional SACs that can simultaneously address the challenges of sulfur side (LiPSs confinement and fast conversion) and lithium metal side (dendrite suppression). The ability of these dual-functional catalysts to simultaneously mitigate the LiPSs shuttle effect and suppress dendrite growth is essential for the next generation Li–S battery systems. However, their integration must be coupled with system-level optimizations, including ultrathin lithium anodes (<50 µm), high-sulfur-loading cathodes (>5 mg cm^{-2}), and lean electrolyte conditions (E/S ratio <3 µL mg^{-1}), to overcome the energy-density–cycle-life trade-off.[4,40]

Herein, we present a facile synthesis method for dual-functional phosphorus-doped iron single-atom catalysts (Fe–NPC) anchored on reduced graphene oxide (rGO), creating a dual-functional nanoreactor (Fe–NPC@rGO) for advanced lithium-sulfur (Li–S) batteries. The material features uniformly dispersed Fe single atoms in a P-coordinated configuration (Fe-N-P-C) within a conductive rGO matrix, confirmed by advanced microscopy and spectroscopy. Density functional theory (DFT) and experiments reveal that Fe–NPC@rGO exhibits both lithiophilic and sulfiphilic properties, enabling efficient sulfur redox catalysis and regulated lithium deposition. As a separator modifier, Fe–NPC@rGO strongly adsorbs and catalyzes lithium polysulfides (LiPSs) (**Scheme 1**), delivering a high discharge capacity of 1156 mAh g^{-1} at 1 C with an ultralow decay rate of 0.032% per cycle over 1000 cycles. Likewise, as a lithium host, it promotes uniform Li nucleation, suppressing dendrites due to its excellent lithiophilic properties. A full battery with Fe–NPC@rGO-Li||Fe–NPC@rGO-PP||ROCNT/S achieves a high areal capacity of 4.9 mAh cm^{-2} under high sulfur loading (5 mg cm^{-2}), low electrolyte/sulfur ratio (6 µL mg^{-1}), and minimal N/P ratio (1.2). Additionally, a pouch cell also displays a high reversible capacity of 976 mA h g^{-1} over 50 cycles at 0.2 C. The outstanding performance stems from the synergistic effects of: (i) the atomic-level dispersion of Fe active sites maximizing catalytic efficiency; (ii) the P-doped coordination environment optimizing electronic structure for both LiPSs conversion and Li deposition; and (iii) the conductive rGO network ensuring efficient electron transport throughout charge/discharge processes. This work demonstrates the potential of dual-functional single-atom catalysts for high-energy Li–S batteries and offers design principles for multifunctional electrocatalysts in complex energy systems.

2. Results and Discussion

2.1. Fabrication and Characterization of Fe–NPC@rGO

As illustrated in **Figure 1a**, Fe–NPC@rGO was synthesized through a straightforward and efficient method. Typically, red phosphorus and formamide (FA) were used as the phosphorus and carbon/nitrogen sources, respectively, while graphene oxide (GO) functioned as the substrate. The synthesis involved a solvothermal treatment at 180 °C, followed by inert annealing at 900 °C. During the solvothermal process, red phosphorous was oxidized by Fe^{3+} and underwent a Shiff–base reaction with FA, facilitating the incorporation of phosphorus near the Fe–N_4 moiety.[41] Meanwhile, a significant amount of Zn^{2+} was introduced into the system to isolate the Fe sites; these ions were subsequently reduced to metallic Zn nanoclusters and evaporated at the high pyrolysis temperature of 900 °C. Additionally, GO was reduced to rGO, partially restoring its high conductivity. Transmission electron microscopy (TEM) images of Fe–NPC@rGO and Fe–NC@rGO (Figure 1b; Figure S1, Supporting Information) clearly show the absence of Fe-derived nanoparticles or clusters on the wrinkled surface of rGO. Corresponding element mapping (Figure 1c) reveals the uniform

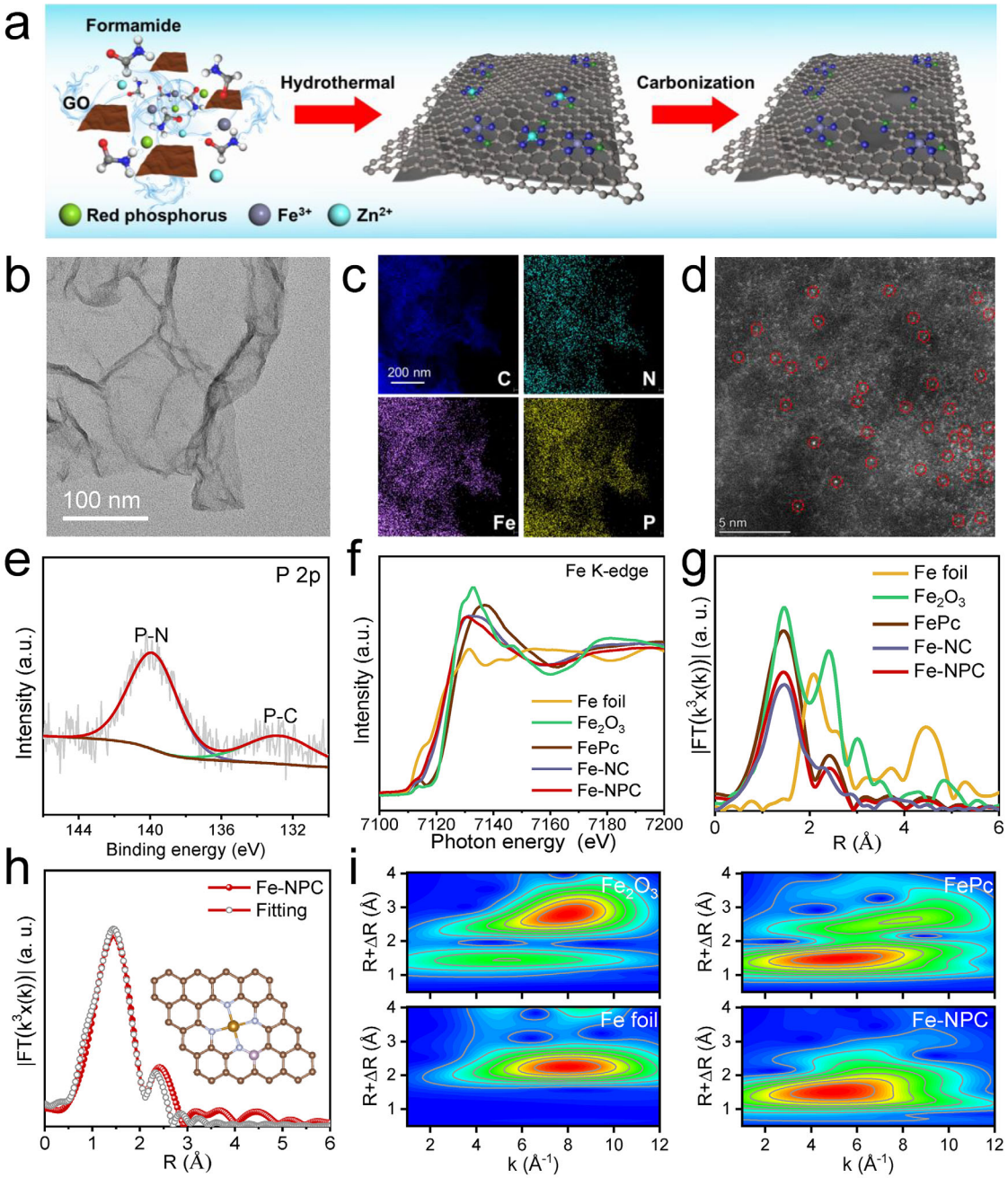

Figure 1. Preparation scheme and characterizations for Fe–NPC@rGO. a) Scheme of the fabrication process of Fe–NPC@rGO. b) TEM image, c) elemental mapping images, and d) HAADF-STEM image of Fe–NPC@rGO. e) High resolution XPS spectra of P 2p, f) Fe K-edge XANES spectra, g) Fe K-edge FT-EXAFS spectra, and h) FT-EXAFS R-space fitting curve of Fe in Fe–NPC@rGO. i) Wavelet transform EXAFS contour plots of Fe–NPC, Fe_2O_3, Fe foil, and FePc.

distribution of Fe, P, N, and C on the rGO substrate. Powder X-ray diffraction (XRD) patterns (Figure S2, Supporting Information) confirm the presence of a purely carbon matrix, with no detectable metal particles in the Fe–NPC@rGO and Fe–NC@rGO.[42] Furthermore, aberration-corrected high angle angular dark field-scanning transmission electron microscopy (HAADF-STEM) images (Figure 1d) show a uniform dispersion of bright dots on rGO, confirming successful fabrication of a monodispersed atomic catalyst in Fe–NPC@rGO. Importantly, a high specific surface area (SSA) and a hierarchical micro/mesoporous structure are critical for facilitating fast redox kinetics, accommodating high sulfur loading, and ensuring efficient electrolyte infiltration.[49] Brunauer-Emmett-Teller (BET) analysis reveals that Fe–NPC@GO exhibits a significantly higher SSA (287 $m^2\ g^{-1}$) compared to Fe–NC@GO (203 $m^2\ g^{-1}$). Furthermore, Barrett-Joyner-Halenda (BJH) pore size distribution confirms

the presence of abundant micropores and mesopores in Fe–NPC@GO, which enhance active site accessibility and ion transport. The larger pore volume compared to Fe–NC@rGO further supports improved sulfur utilization and reduced polysulfide shuttling, leading to superior cycling stability and rate capability (Figure S3, Supporting Information).

To elucidate the local structure and coordination environment of Fe–NPC@rGO, we conducted comprehensive analysis using X-ray photoelectron spectroscopy (XPS), X–ray absorption near–edge structure (XANES), and extended X–ray absorption fine structure (EXAFS) techniques. The P 2p XPS spectra of Fe–NPC@rGO (Figure 1e) exhibit two prominent peaks at 140.0 eV and 132.9 eV, corresponding to P—N and P—C bonds, respectively,[43] indicating successful incorporation of phosphorus into carbon matrix with significant P–N bonding. Additionally, analysis of the Fe 2p XPS spectra indicates presence of metal species in their ionic forms (Figure S4, Supporting Information). Furthermore, inductively coupled plasma optical emission spectroscopy (ICP-OES) was employed to determine the content of Fe atoms in Fe–NC@rGO (3.14 wt%) and Fe–NPC@rGO (4.29 wt%). The Fe K-edge XANES spectra (Figure 1f) were benchmarked against reference spectra of Fe foil, Fe_2O_3, and iron phthalocyanine (FePc), revealing that the Fe species in Fe–NPC@rGO possess a mixed valence state between +2 and +3.[44,45] Further insight into the Fe coordination environment was obtained through Fourier transform analysis of EXAFS (FT–EXAFS), which showed a dominant peak at 1.45 Å, attributed to Fe–N coordination in the first shell, with no detectable Fe—Fe bonding (Figure 1g). The absence of Fe—Fe bonding corroborates the atomic dispersion of Fe sites within the rGO matrix. Detailed EXAFS fitting (Figure 1h and Table S1, Supporting Information) confirmed that each Fe atom is coordinated by four N atoms, forming an Fe-N4 moiety, while phosphorus doping is evidenced by the Fe–N–P–C configuration. To further delineate the coordination environment, wavelet transform (WT) EXAFS analysis was employed, providing a nuanced visualization of scattering contribution in both k and R space. As shown in Figure 1i, the WT-EXAFS contour plots for Fe–NPC@rGO distinctly differ from those of Fe foil, aligning more closely with FePc, thus reinforcing the absence of Fe—Fe bonds and the presence of Fe–N coordination. In exploring the feasibility of phosphorus doping, DFT calculations were conducted to evaluate the formation energies of seven potential P-doping sites (Figures S5,S6, Supporting Information). The results identified the Fe–N–P–C configuration (referred to as P1) as the most thermodynamically favorable, consistent with experimental observations. These findings substantiate the atomic dispersion of Fe–N_4–P sites and validate the strategic incorporation of phosphorus, significantly advancing our understanding of the local structural environment in single-atom catalysts (SACs).

2.2. Adsorption and Electrocatalytic Effects of Fe–NPC@rGO on LiPSs

To evaluate the sulfur trapping capabilities of Fe–NPC@rGO, we conducted a visual adsorption test by immersing equal masses of various samples in a Li_2S_6 solution (dissolved in DOL/DME) for 6 hours. Remarkably, the Fe–NPC@rGO sample transformed the solution color from yellow to nearly transparent, whereas the Fe–NC@rGO sample only caused a color transition to pale yellow. This stark contrast highlights the superior adsorption capacity of Fe–NPC@rGO. UV/vis spectra (**Figure 2a**) further corroborate this observation, demonstrating that Fe–NPC@rGO has a stronger chemical affinity and higher adsorption capacity for LiPSs. Investigating the intrinsic catalytic effects of Fe–NPC@rGO and Fe–NC@rGO on the conversion of LiPSs, we measured cyclic voltammetry (CV) profiles of Li_2S_6 symmetrical cells. These cells used identical electrodes for both the cathode and anode, with 0.1M Li_2S_6 electrolyte as the active materials. As shown in Figure 2b, the CV profiles display two pairs of redox peaks, corresponding to the reversible conversions between S_8, Li_2S_6, and Li_2S. Compared to the Fe–NPC@rGO electrode, the symmetric cell using the Fe–NC@rGO electrode exhibits a lower current response with no distinct redox peaks and a higher voltage hysteresis between the cathode and anode potentials. This observation indicates that Fe–NPC@rGO exhibits superior catalytic effects on the electrochemical conversion of LiPSs, likely due to the induced P in Fe–N_4 moiety. The reduction of liquid Li_2S_4 to solid Li_2S, which accounts for three-quarters of the theoretical capacity, is crucial for ensuring high sulfur utilization.[46] To evaluate the Li_2S nucleation, potentiostatic measurements were performed using carbon paper electrodes coated with Fe–NPC@rGO and Fe–NC@rGO as cathodes. As shown in Figure 2c, the Fe–NPC@rGO electrode facilitated accumulated Li_2S precipitation capacities up to 378 mAh g^{-1}, significantly surpassing 292 mAh g^{-1} observed for Fe–NC@rGO. This substantial improvement highlights the superior capability of Fe–NPC@rGO in reducing the energy barrier for LiPSs conversion and promoting Li_2S nucleation and growth. These findings highlight the potential of Fe–NPC@rGO as an effective material for enhancing sulfur utilization and improving the overall performance of Li–S batteries through efficient sulfur trapping and conversion processes.

XPS was utilized to explore the interaction between LiPSs and Fe–NPC@rGO. Figure 2d displays the high-resolution N 1s XPS spectra, revealing the presence of pyridinic N, pyrrolic N, graphitic N, and N–O groups in Fe–NPC@rGO, with pyridine being dominant. This pyridinic N is known to coordinate with metal ions.[35,37] In the Fe 2p spectra (Figure 2e,f), both Fe–NC@rGO and Fe–NPC@rGO exhibit the characteristic peaks of Fe $2p_{3/2}$ and Fe $2p_{1/2}$ orbitals. Notably, Fe–NPC@rGO are shifted by 0.3 eV toward lower binding energies compared to Fe–NC@rGO, indicating that the incorporation of phosphorus leads to a higher proportion of Fe in a reduced state. Upon adsorption of Li_2S_6, the Fe 2p peaks in Fe–NPC@rGO and Fe–NC@rGO shift further by 0.7 and 0.4 eV, respectively, toward lower binding energies. This suggests that the neighboring incorporation of P atom results in a greater proportion of Fe components in their reduced states in Fe–NPC@rGO. The S 2p spectra (Figure 2g) show a 1:2 ratio of the $2p_{3/2}$ contributions at 161.7 eV and 163.1 eV, which corresponded to terminal (S_T^{-1}) and bridging sulfur (S_B^0) atoms, respectively.[47] The S 2p peaks of Fe–NPC@rGO appear at higher binding energies compared to those of Li_2S_6 on Fe–NC@rGO, further confirming stronger chemical interaction between Fe–NPC@rGO and Li_2S_6.

To validate the practical applicability of Fe–NPC@rGO, we engineered a functional separator by coating the composite

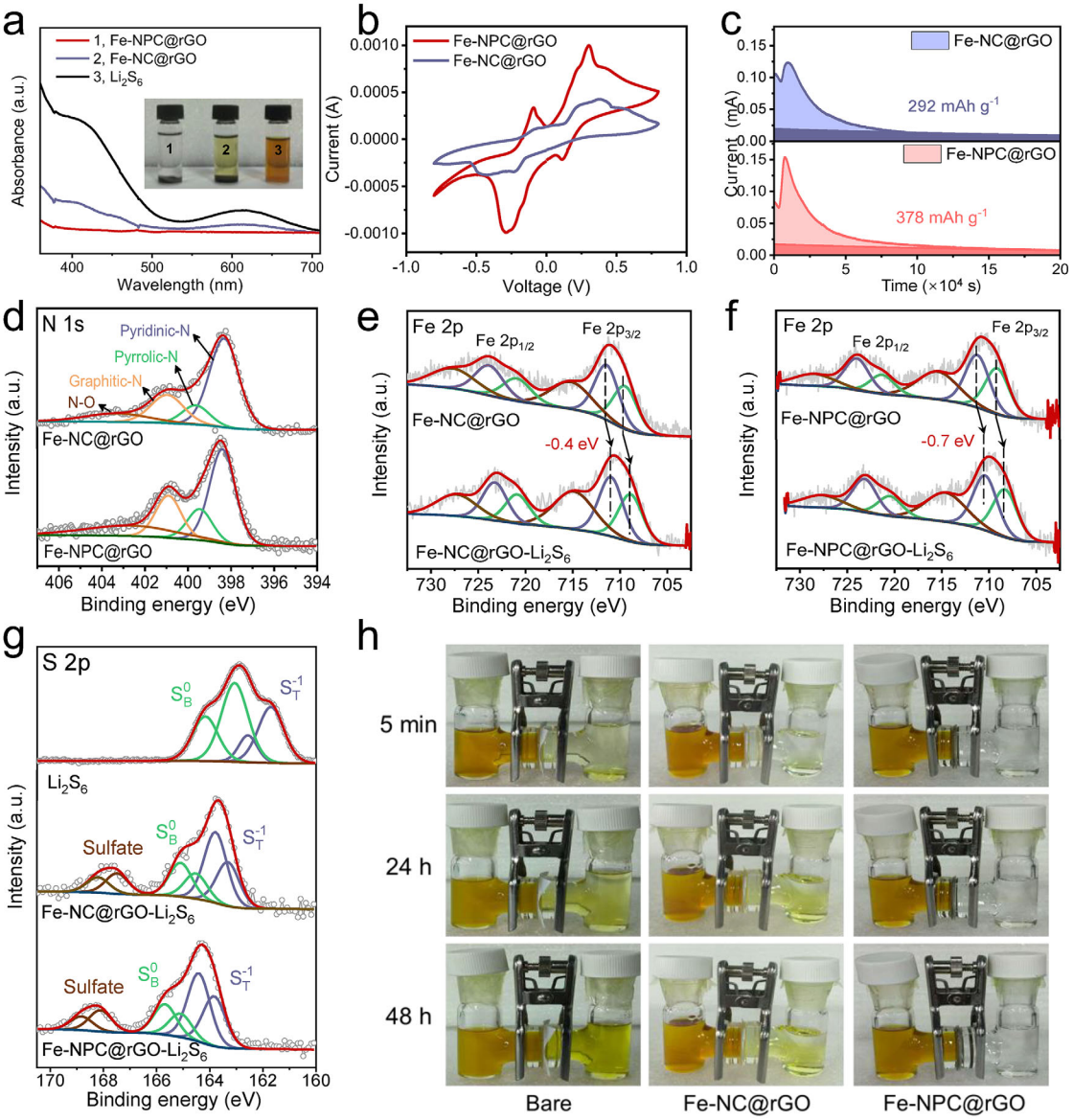

Figure 2. Demonstration of the strong interaction of LiPSs with Fe–NPC@rGO. a) UV–vis spectroscopy of Li_2S_6 solutions (the inset is the digital photographs of the Li_2S_6 solution after adding Fe–NPC@rGO and Fe–NC@rGO for 6 h). b) CV curves of symmetric cells from −0.8 to 0.8 V at a scan rate of 0.1 mV s^{-1}. c) Li_2S nucleation test for Fe–NPC@rGO and Fe–NC@rGO. XPS study of Fe–NPC@rGO and Fe–NC@rGO samples before and after interacting with Li_2S_6. XPS spectrum of d) N 1s, e, f) Fe 2p, and g) S 2p. h) Diffusion tests of LiPSs with bare, Fe–NC@rGO, and Fe–NPC@rGO modified separators.

materials on to a commercial Celgard polypropylene (PP) separator (areal loading: 0.45 mg cm^{-2}) (Figure S7, Supporting Information). The resulting Fe–NPC@rGO/PP separator presents favorable flexibility and durability, without crack or delamination after bending and restoring (Figure S8, Supporting Information). H-cell diffusion tests with 5 mM Li_2S_6 electrolyte revealed striking differences in LiPSs blocking capability. As shown in Figure 2h, LiPSs easily escape through bare separator, turning the right chamber completely yellow after 48 hours. The Fe–NC@rGO/PP separator mitigated LiPSs shuttling to some extent, there was still significant diffusion of LiPSs from left chamber to pure electrolyte in the right chamber. In sharp contrast, the Fe–NPC@rGO/PP separator exhibited impressive LiPSs blocking capability, maintaining the right chamber colorless and transparent after long time diffusion test, validating its effectiveness in preventing polysulfide shuttling and enhancing the stability of Li–S batteries.

To elucidate the electrocatalytic mechanism of phosphorus-modulated Fe–N_4 sites toward LiPSs, systematic density functional theory (DFT) calculations were conducted with van der Waals corrections (DFT-D3 method) to account for non-covalent interactions. Two representative models were constructed, i) Fe–N_4–P coordinated structure (Fe–NPC) mimicking the phosphorus-doped configuration and ii) conventional

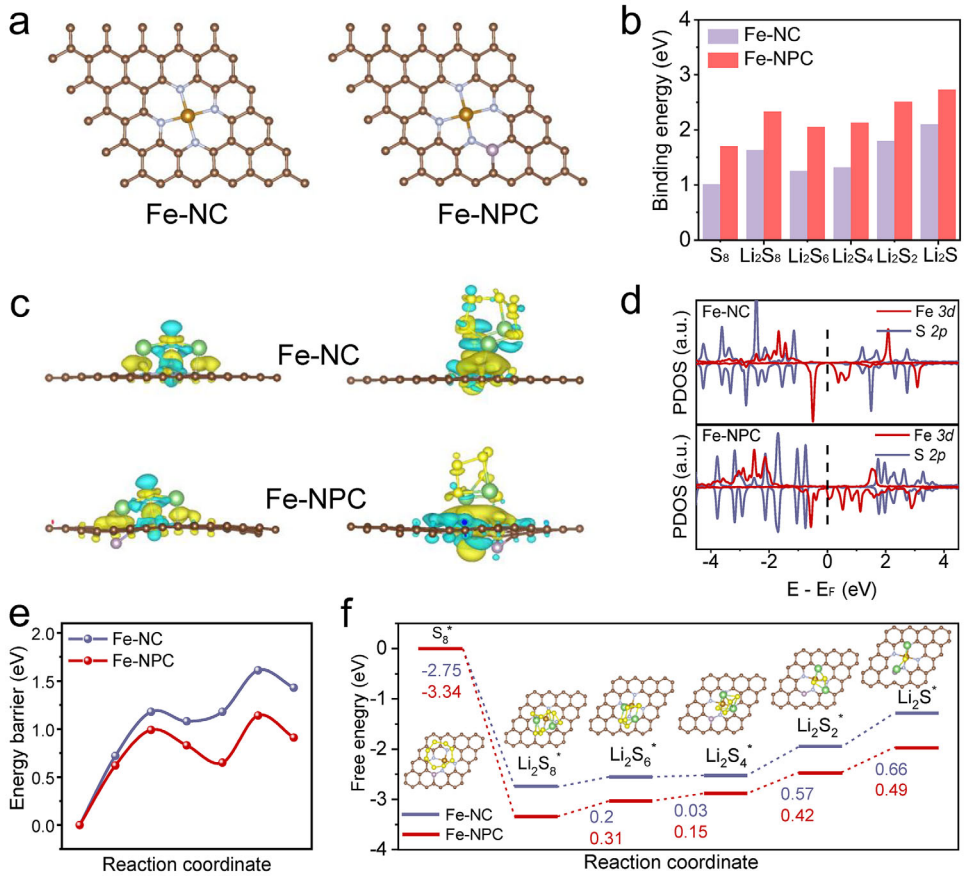

Figure 3. The theoretical calculation of chemical interaction between LiPSs and Fe–NPC. a) Structures of Fe–NC and Fe–NPC used in first-principles calculations. b) Binding energy between the LiPSs and Fe–NC and Fe–NPC. c) The charge density difference of Li_2S/Li_2S_6 adsorption on Fe–NC and Fe–NPC. d) DOS of Li_2S_6 adsorption on Fe–NC or Fe–NPC. e) The decomposition energy barriers of Li_2S on the surface of Fe–NC and Fe–NPC. f) Energy profiles for the reduction of LiPSs on Fe–NC and Fe–NPC.

$Fe–N_4$ structure (Fe–NC) as the reference (**Figure** 3a). The adsorption energetics were quantitatively evaluated through binding energy (E_b) calculations: $E_b = E_{substrate} + E_{li2Sx} - E_{li2Sx@substrate}$, where E represents the total energy of each component. As shown in Figure 3b; Figure S9 (Supporting Information), Fe–NPC exhibits 30–68% stronger binding energies (1.7–2.73 eV) with various LiPSs compared to Fe–NC (1.01–2.1 eV), demonstrating significantly enhanced chemisorption capability. Figure 3c shows the charge density difference plot of Li_2S and Li_2S_6 adsorbed on Fe–NC and Fe–NPC, respectively. The charge distribution pattern reveals enhanced electron accumulation between Li_2S/Li_2S_6 and Fe–NPC. This intensified electron donation originates from the P-induced electronic structure modulation, where the neighboring P atoms lowers the Fe-3d band center, facilitating electron migration to antibonding orbitals of Li–S species. Projected density of states (PDOS) analysis further confirms strengthened interfacial interactions. The hybridized states between S-3p and Fe-3d orbitals near the Fermi level (-1.5 to 0.5 eV) show 38% greater orbital overlap in Fe-NPC compared to Fe–NC (Figure 3d), suggests faster electron transfer between the $Fe–N_4–P$ sites and Li_2S_6, thus facilitating the accelerated electrochemical conversion of LiPSs.

The decomposition energy barriers on different substrates were computed using climbing-image nudged elastic band (CI-NEB) method. Fe–NPC reduces the Li_2S dissociation barrier to 1.14 eV versus 1.61 eV for Fe–NC (Figure 3e), indicating 29.2% lower activation energy for Li–S bond cleavage.[48] Gibbs free energy profiles (Figure 3f) unveil the rate-limiting step (RDS) is the transition from $*Li_2S_2$ to $*Li_2S$.[49] The Gibbs free energy for RDS is substantially lower on Fe–NPC (0.49 eV) compare to that of Fe-NC (0.66 eV), indicates that the reduction of sulfur is more favorable on Fe–NPC. This thermodynamic facilitation aligns well with experimental symmetric CV and Li_2S nucleation tests, which contributes to the high sulfur utilization and excellent cyclic stability of Li–S batteries.

Li–S coin cells were assembled with lithium metal foil anodes, ROCNT-S composite cathodes, and functionalized separators (bare PP, Fe–NC@rGO/PP, or Fe–NPC@rGO/PP). CV analysis at 0.1 mV S^{-1} reveals critical kinetic differences (**Figure** 4a):

Reduction process:

$$\text{Peak } C_1 \text{ (2.30 V)}: \text{ Solid} - \text{liquid conversion}$$

$$(S_8 \rightarrow Li_2S_x, 4 \leq x \leq 8) \quad (1)$$

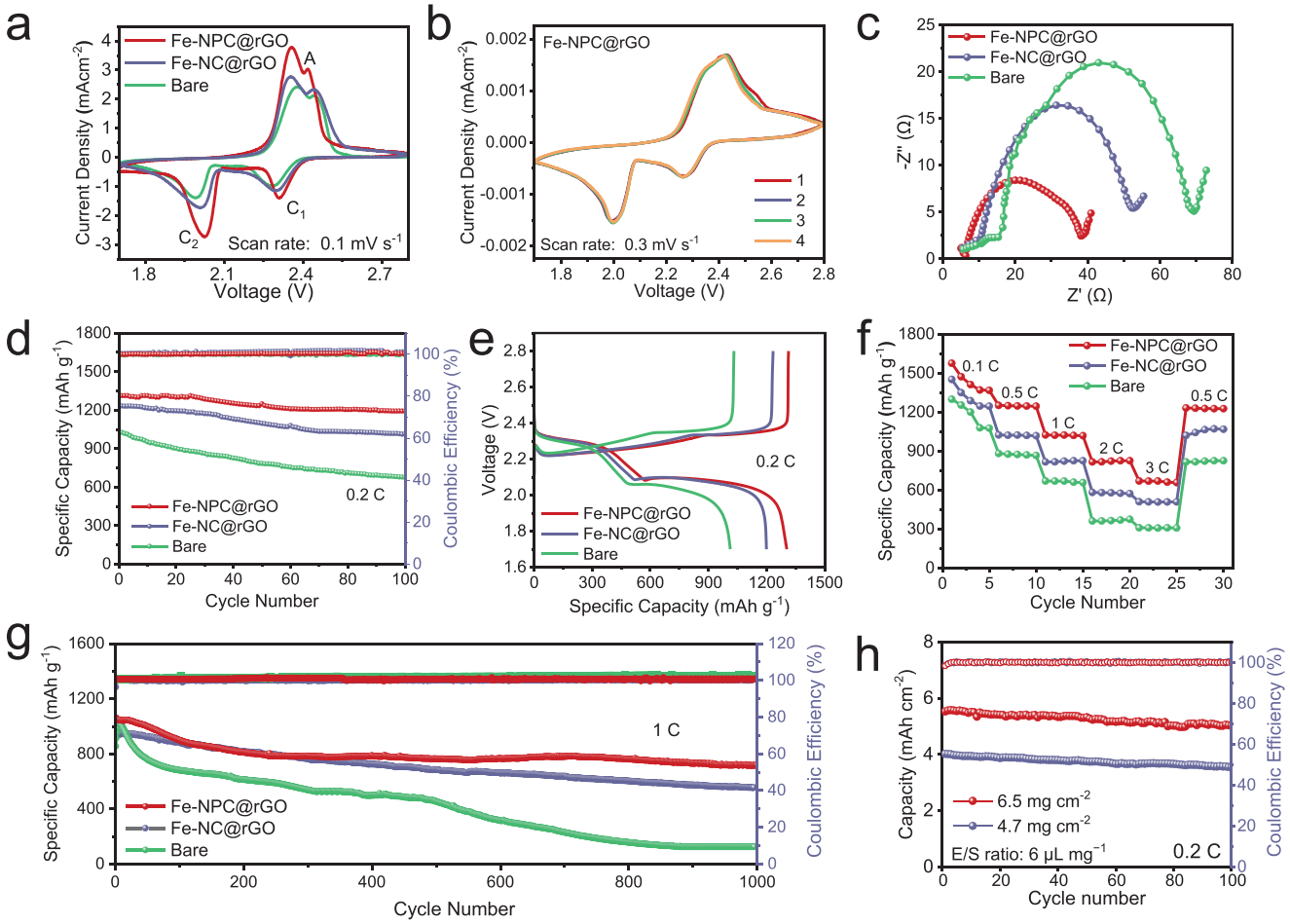

Figure 4. Electrochemical performance of Li–S cells using different separators. a) CV curves of Li–S cells at a scanning rate of 0.1 mV s^{-1} in a voltage range of 1.7–2.8 V. b) CV curves of Fe–NPC@rGO cell. c) Electrochemical impedance spectra of the Li–S cells. d) Cyclic performance at 0.2 C, e) charge/discharge profiles, f) rate performance at various cycling rates, g) long-term cycling performance at 1 C of the Li–S cells using different separators. h) Cycling performance of Fe–NPC@rGO cells with high sulfur loading and low E/S ratio at 0.2 C.

$$\text{Peak } C_2 \text{ (2.05 V)}: \text{ Solid} - \text{sate nucleation } (Li_2S_x \rightarrow Li_2S_2/Li_2S) \quad (2)$$

Oxidation process:

Peak A_1/A_2 (2.35/2.45 V): Delithiation of Li_2S through short-chain LiPSs intermediates.

Notably, the CV profile of the Fe–NPC@rGO separator exhibits the highest current density and the lowest voltage gap compared to Fe–NC@rGO, confirming significantly enhanced conversion kinetics of sulfur species. Furthermore, the redox peaks in CV curves for the Fe–NPC@rGO separator remain almost overlapping across the first, second, third, and fourth cycles (Figure 4b), indicating a highly reversible redox reaction and excellent cycling stability. Electrochemical impedance spectroscopy (EIS) results, shown in Figure 4c, reveal a smaller interfacial charge transfer resistance for the cell using Fe–NPC@rGO separator, indicating faster electron and lithium-ion transport.

The electrochemical superiority of Fe–NPC@rGO was systematically evaluated in Li–S coin cells configured with sulfur cathodes (2 mg cm^{-2}) and different separators. At 0.2 C, cells employing the Fe–NPC@rGO separator delivered an initial discharge capacity up to 1313 mAh g^{-1} with 90.9% retention after 100 cycles (1193 mAh g^{-1}), significantly outperforming Fe–NC@rGO (82.4%) and bare PP (66%), corresponding to capacity decay rates of 0.091%, 0.176%, and 0.34% per cycle, respectively (Figure 4d). This enhanced cyclability stems from the synergistic effects of strong LiPSs chemisorption on Fe–NPC@rGO (DFT: 2.05 eV binding energy for Li_2S_6) and accelerated conversion kinetics, as evidenced by the reduction in charge-discharge voltage hysteresis (Figure 4e). Rate capability testing revealed exceptional sulfur utilization across current densities, maintaining 42.5% capacity at 3.0 C (670 vs. 1576 mAh g^{-1} at 0.1 C) with 98.4% polarization recovery upon reverting to 0.5 C (1232 mAh g^{-1}, Figure 4f). The corresponding galvanostatic charge–discharge curves at different current densities are shown in Figure S10 (Supporting Information). Long term cycling at 1.0 C (Figure 4g) demonstrated unprecedented stability for the cells using Fe–NPC@rGO modified separator, retaining 76.5% of initial capacity (1061 mAh g^{-1}) after 1000 cycles with a negligible decay rate of 0.032% per cycle—metrics that surpass state-of-the-art metal-nitrogen-carbon catalysts (Tables S2,S3, Supporting Information). In contrast, the cell with the Fe–NC@rGO

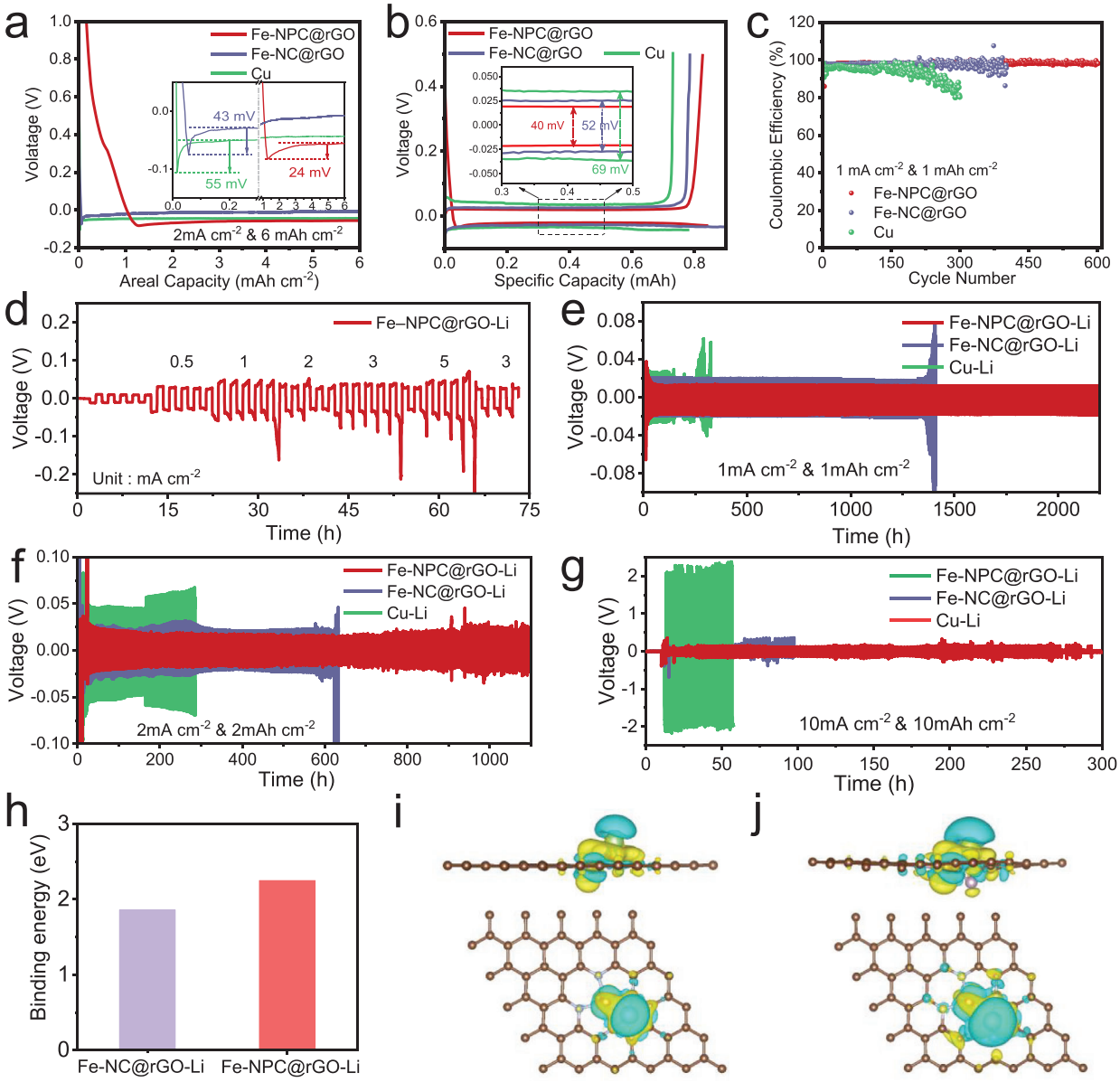

Figure 5. Lithium dendrite suppression of Fe–NPC@rGO. a) Voltage profiles for Li plating-stripping (Insets are amplified galvanostatic discharge curves). b) Corresponding voltage profiles of the different electrodes under a deposition capacity of 2.0 mAh cm^{-2} at 6 mA cm^{-2}. c) Coulombic efficiencies of Li||Cu half cells with the Li deposition capacities of 1 mA cm^{-2} and current density of 1 mA cm^{-2}. d) Rate performances of the symmetric cells at different current densities from 0.5 to 5 mA cm^{-2}. Cycling performance of symmetric cells using Fe–NPC@rGO–Li, Fe–NC@rGO–Li, and Cu–Li e) 1 mA cm^{-2}, f) 2 mA cm^{-2}, and g) 10 mA cm^{-2}. h) Binding energy of Li with Fe–NC and Fe–NPC. The charge density difference of Li atom adsorption on i) Fe–NC and j) Fe–NPC.

separator exhibits a gravimetric capacity of 930 mAh g^{-1}, with a capacity fading rate of 0.041% per cycle. Practical viability was further validated under stringent conditions: At elevated sulfur loadings (4.7 and 6.5 mg cm^{-2}) and lean electrolyte (E/S = 6 μL mg^{-1}), the system achieved a high areal capacity of 4 and 5.5 mAh cm^{-2} at 0.2 C with 100 stable cycles (Figure 4h). These collective advance Fe-NPC@rGO as a transformative separator technology that concurrently address sulfur utilization, reaction kinetics, and scalability challenges in practical Li–S batteries.

2.3. Lithium Dendrite Suppression of Fe–NPC@rGO

The Fe–NPC@rGO architecture demonstrates unprecedented dual functionality in Li–S batteries, simultaneously addressing LiPSs shuttling and lithium dendrite growth. As shown in **Figure 5a**, Fe–NPC@rGO exhibits the lowest overpotential for Li nucleation (24 mV), 48% and 63% lower than Fe–NC@rGO (46 mV) and planar Cu (65 mV), respectively. Furthermore, Fe–NPC@rGO presents the least polarization among the three electrodes in voltage-capacity comparison (Figure 5b), with a

steady overpotential of just 40 mV. These results suggest that Fe–NPC@rGO can rapidly absorb Li ions, while preventing Li atoms from migrating freely through the steric effect, thereby promoting homogeneous lithium deposition and ultimately suppressing Li dendrite formation. The Coulombic efficiency (CE) of Li||Cu half-cells was used to study the stability of Li metal anodes. As shown in Figure 5c, the CE of Li plating at a current density of 1 mA cm^{-2} and a capacity of 1 mAh cm^{-2} on the Fe–NPC@rGO electrode stabilizes at 98.2% after 600 cycles, whereas the Fe–NC@rGO electrode stabilizes at 97.6% after 400 cycles. The planar Cu electrode shows a lower CE of 93.3% after 300 cycles, due to irreversible Li depletion from the formation of unstable SEI or "dead Li". Notably, at a current density of 0.5 mA cm^{-2}, the Fe–NPC@rGO electrode maintains an average CE of 98.5% after 900 cycles (Figure S11, Supporting Information).

The rate performance of the Fe–NPC@rGO–Li electrode was tested at a fixed capacity of 0.5 mAh cm^{-2} with current densities ranging from 0.5 to 5 mA cm^{-2} in symmetric cells (Figure 5d). The Fe–NPC@rGO–Li electrode exhibits stable cycling with a consistent voltage plateau at 5 mA cm^{-2}, attributed to its ability to promote homogeneous lithium deposition. To further verify the electrochemical cycling stability of the Fe–NPC@rGO–Li electrode, the interfacial stability of the Li metal anode during repeating charge/discharge processes was tested. As shown in Figure 5e, the Fe–NPC@rGO–Li symmetrical cell exhibits stable cycle over 2200 h, with a steady voltage during the charge/discharge process at a current density of 1mA cm^{-2} and a plating capacity of 1 mAh cm^{-2}. In contrast, the Fe–NC@rGO–Li (1300 h) and Cu–Li electrodes (250 h) show limited cycling life with fluctuating voltage hysteresis, attributed to dendrite formation and "dead Li" accumulation during the lithium plating/stripping process. At a higher current density of 2.0 mA cm^{-2} and a plating capacity of 2 mAh cm^{-2}, the Fe–NPC@rGO–Li symmetrical cell demonstrated robust cycling stability for over 1200 h, while Fe–NC@rGO–Li and Cu–Li electrodes survived only 600 and 300 h, respectively (Figure 5f). Notably, at higher current densities of 10.0 mA cm^{-2} and a plating capacity of 10 mAh cm^{-2}, the Fe–NPC@rGO–Li electrode maintains a stable voltage plateau and low overpotential, further demonstrating that Fe–NPC@rGO effectively regulates Li deposition and suppresses dendrite formation (Figure 5g).

The Li deposition behavior varied significantly across the three hosts (Cu-Li, Fe–NC@rGO-Li, and Fe–NPC@rGO-Li). To analyze surface morphology deposition behavior, different hosts Li-Li symmetric cells were assembled and examined via SEM imaging at 1.0 mA cm^{-2}/1.0 mAh cm^{-2}. The Cu-Li host exhibited severe degradation, with porous and dendritic Li deposits (Figure S12a, Supporting Information). In contrast, the Fe–NC@rGO-Li host demonstrated improved uniformity due to its conductive nitrogen-doped carbon framework, which facilitated better Li^+ distribution. However, after prolonged cycling, a coarse surface and eventual dendrite formation was observed (Figure S12b, Supporting Information). Remarkably, the Fe–NPC@rGO-Li host maintained a smooth and dense Li morphology after 100 h (Figure S12c, Supporting Information). The key difference lies in phosphorus doping, which enhances lithiophilicity through strong Li-N interactions. Additionally, the N, P-coordinated Fe sites contribute to a more stable artificial SEI, preventing electrolyte decomposition and reducing inhomogeneous Li^+ flux. This functionality—and interfacial stabilization—explains the superior cycling stability of Fe–NPC@rGO compared to its undoped counterpart (Fe–NC@rGO) and the uncontrolled Cu-Li system.

To evaluate the feasibility of practical application, we fabricated full cells with Fe–NPC@rGO–Li anodes (3 mAh cm^{-2}) and $LiFePO_4$ (LFP) cathodes. As shown in Figure S13 (Supporting Information), the Fe–NPC@rGO–Li||LFP cell shows excellent rate performance. The Fe–NPC@rGO–Li||LFP full cells deliver reversible capacities of 169, 158, 146, 132, and 102 mAh g^{-1} at 0.1, 0.5, 1, 2, and 5 C rates, respectively. When the rate is restored to 1 C, the specific capacity almost recovers to the original value, indicating that Fe–NPC@rGO–Li anode increases the utilization rate of Li metal, thereby improving cell reversibility. Even at a high current density of 3 C, the Fe–NPC@rGO–Li||LFP full battery still delivers a high reversible capacity of 143 mAh g^{-1}, maintaining 114 mAh g^{-1} after 500 cycles with a capacity fading rate of 0.041% per cycle (Figure S14, Supporting Information). These results underscore the effectiveness of Fe–NPC@rGO in enhancing the performance and durability of Li metal batteries, even under demanding conditions. Furthermore, DFT calculations demonstrate that the Li adsorption energy on Fe–NPC (−2.25 eV) is greater than that on Fe–NC (−1.86 eV) (Figure 5h). The charge density difference analysis (Figure 5i,j) reveals that Li atoms prefer to nucleate around the Fe–N_4–P sites, indicating that Fe–NPC provides sufficient Li nucleation sites for uniform Li deposition.

2.4. Performance of Fe–NPC@rGO-Li||Fe–NPC@rGO-PP||ROCNT-S Full Battery

Based on the well-designed properties of dual-functional nanoreactors for both the separator and the anode, the developed Fe–NPC@rGO-Li anode, Fe–NPC@rGO separator, and ROCNT-S cathode were coupled as a Li–S full battery (Fe–NPC@rGO-Li||Fe–NPC@rGO-PP||ROCNT-S) to indicate their potential for practical applications. A key factor for achieving high performance in the battery industry is a low area capacity ratio of the negative to positive electrodes (N/P). The Fe–NPC@rGO-Li anode with a capacity of 10 mA h cm^{-2} was paired with the ROCNT-S cathode with a mass loading of 2 mg cm^{-2} (3.3 mA h cm^{-2}) in full batteries (**Figure 6a**). The full cell with a low N/P ratio of 3 showed excellent cycling performance at 1 C, which maintained 76.2% of the original discharge capacity after 300 cycles. For practical high-energy-density Li–S batteries, a high S loading cathode, low N/P ratio, and lean electrolytes are essential.[40] To further demonstrate the superiority of the Fe–NPC@rGO-Li||Fe–NPC@rGO-PP||ROCNT-S full battery, a low electrolyte-to-sulfur (E/S) ratio of 6 µL mg^{-1}, and high sulfur areal loadings of 3.7 and 5 mg cm^{-2}, corresponding N/P ratios of 1.6 and 1.2, respectively, were assembled. As shown in Figure 6b, areal capacities of 3.3 and 4.9 mAh cm^{-2} were achieved, with superior cycling stability over 100 cycles and nearly 100% Coulombic efficiency at 3.7 and 5 mg cm^{-2}, respectively. This demonstrated higher sulfur utilization and enhanced electrochemical kinetics in the full batteries. To further explore the practical

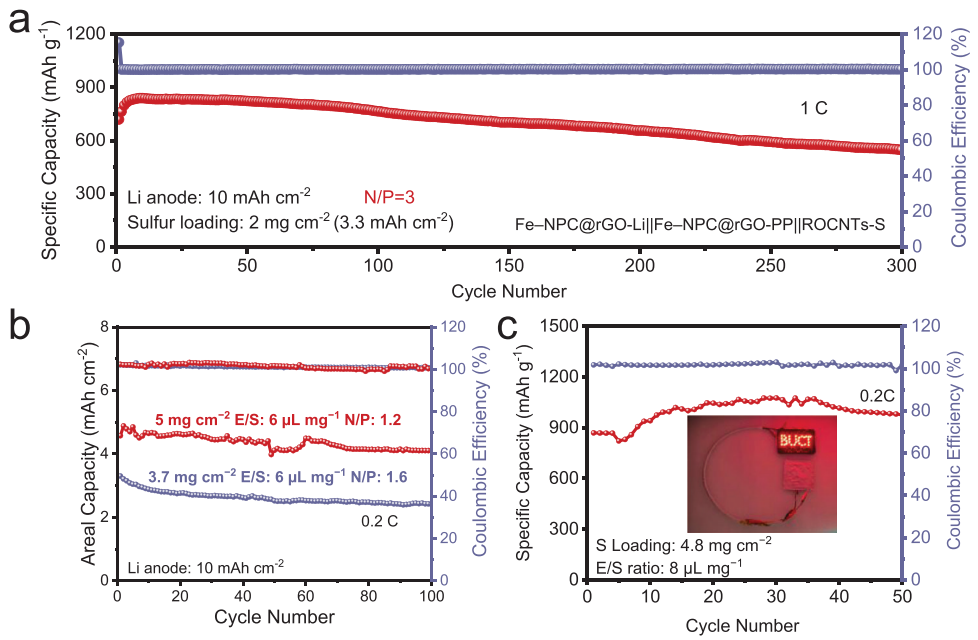

Figure 6. Electrochemical performance of Fe–NPC@rGO-Li||Fe–NPC@rGO-PP||ROCNT-S full battery. a) Long-term cycling performance of full cell with low E/S ratio at 1 C. b) Cycling performance of full cells with high sulfur loading, low E/S ratio, and low N/P ratio at 0.2 C. c) Cycling performance of a Li–S pouch cell at 0.2 C (the inset demonstrates the digital picture of Li–S pouch cell powering LED lights).

applicability of Fe–NPC@rGO-Li separator and Fe–NPC@rGO-Li anode, a Li–S pouch cell was fabricated. Notably, the pouch cell delivered a reversible capacity of 976 mA h g^{-1} over 50 cycles at 0.2 C (Figure 6c), which was capable of powering a set of LED lights displaying the "BUCT" logo with ease.

3. Conclusion

In summary, this work establishes phosphorus-doped Fe–N_4 single-atom catalysts (SACs, Fe–NPC@rGO) as dual functional electrocatalyst revolutionizing Li–S battery architecture. Through electronic structure engineering, Fe–NPC@rGO concurrently addresses two fundamental challenges: 1) Strong LiPSs chemisorption (2.05 eV binding energy) and efficient catalysis (0.49 eV barrier in RDS), which enables sulfur cathode with a high discharge capacity of 1156 mAh g^{-1} and 1000-cycle stability at 1 C with 0.032% decay rate, and 2) lithiophilic nucleation sites drive dendrite free operation even at ultrahigh current density (10 mA cm^{-2}). The integrated Fe–NPC@rGO-Li||Fe–NPC@rGO-PP||ROCNT-S full cell achieves paradigm-shifting metrics—high areal capacity of 4.9 mAh cm^{-2} at N/P = 1.2 and E/S = 6—while pouch cell validation (976 mA h g^{-1} over 50 cycles at 0.2 C) bridges laboratory innovation to commercial viability. This cathode/anode optimization strategy with dual functional SACs electrocatalyst opens avenues for developing energy-dense, lean-electrolyte battery systems.

Supporting Information

Supporting Information is available from the Wiley Online Library or from the author.

Acknowledgements

A.H.P. and L.R. contributed equally to this work. This work was financially supported by the National Natural Science Foundation of China (22479007, 21771018, 21875004, 22108149), Beijing University of Chemical Technology (buctrc201901) and Beijing Municipal Natural Science Foundation (2192037).

Conflict of Interest

The authors declare no conflict of interest.

Data Availability Statement

The data that support the findings of this study are available from the corresponding author upon reasonable request.

Keywords

electro-catalysis, iron Single atomic catalyst, lithium–sulfur batteries, lithium dendrites, polysulfides redox kinetics, shuttle effect

Received: March 20, 2025
Revised: May 30, 2025
Published online:

[1] Y. Yang, G. Zheng, Y. Cui, *Chem. Soc. Rev.* **2013**, *42*, 3018.
[2] A. Manthiram, Y. Fu, S. H. Chung, C. Zu, Y. S. Su, *Chem Rev.* **2014**, *114*, 11751.
[3] Z. W. Seh, Y. Sun, Q. Zhang, Y. Cui, *Chem. Soc. Rev.* **2016**, *45*, 5605.
[4] B. Liu, R. Fang, D. Xie, W. Zhang, H. Huang, Y. Xia, X. Wang, X. Xia, J. Tu, *Energy Environ. Mater.* **2018**, *1*, 196.

[5] L. Ren, J. Liu, A. H. Pato, Y. Wang, X. Lu, I. A. Chandio, M. Zhou, W. Liu, H. Xu, X. Sun, *Mater. Futur.* **2023**, *2*, 042103.
[6] B. Liu, J.-G. Zhang, W. Xu, *Joule* **2018**, *2*, 833.
[7] P. Bonnick, J. Muldoon, *Energy Environ. Sci.* **2020**, *13*, 4808.
[8] R. Fang, S. Zhao, Z. Sun, D. W. Wang, H. M. Cheng, F. Li, *Adv. Mater.* **2017**, *29*, 1606823.
[9] Y. Chen, T. Wang, H. Tian, D. Su, Q. Zhang, G. Wang, *Adv. Mater.* **2021**, *33*, 2003666.
[10] D. Lin, Y. Liu, Y. Cui, *Nat. Nanotechnol.* **2017**, *12*, 194.
[11] C. Yan, X.-B. Cheng, C.-Z. Zhao, J.-Q. Huang, S.-T. Yang, Q. Zhang, *J. Power Sources* **2016**, *327*, 212.
[12] H. Yang, C. Guo, A. Naveed, J. Lei, J. Yang, Y. Nuli, J. Wang, *Energy Storage Mater.* **2018**, *14*, 199.
[13] Y. Huang, L. Lin, Y. Zhang, L. Liu, B. Sa, J. Lin, L. Wang, D. L. Peng, Q. Xie, *Nanomicro. Lett.* **2023**, *15*, 67.
[14] R. Zhou, Y. Ren, W. Li, M. Guo, Y. Wang, H. Chang, X. Zhao, W. Hu, G. Zhou, S. Gu, *Angew. Chem., Int. Ed.* **2024**, *63*, 202405417.
[15] H. Shi, X. Ren, J. Lu, C. Dong, J. Liu, Q. Yang, J. Chen, Z. S. Wu, *Adv. Energy Mater.* **2020**, *10*, 2002271.
[16] S. Fu, H. Wang, Y. Zhong, S. Schaefer, M. Li, M. Wu, H. Wang, *Adv. Mater.* **2023**, *35*, 2302771.
[17] L. Ren, L. Qiao, A. H. Pato, J. Liu, Y. Wang, X. Lu, Y. Zhao, Q. Wang, W. Liu, H. Xu, X. Sun, *J. Mater. Chem. A* **2024**, *12*, 4249.
[18] L. Qiao, L. Ren, R. Zhang, J. Chen, M. Xu, J. Liu, H. Xu, W. Liu, Z. Chang, X. Sun, *Energy Fuels* **2021**, *35*, 10219.
[19] L. Ren, Q. Wang, Y. Li, C. Hu, Y. Zhao, L. Qiao, H. Zhou, W. Liu, H. Xu, X. Sun, *Inorg. Chem. Front.* **2021**, *8*, 3066.
[20] R. Wang, J. Qin, F. Pei, Z. Li, P. Xiao, Y. Huang, L. Yuan, D. Wang, *Adv. Funct. Mater.* **2023**, *33*, 2305991.
[21] J. Liu, D. G. D. Galpaya, L. Yan, M. Sun, Z. Lin, C. Yan, C. Liang, S. Zhang, *Energy Environ. Sci.* **2017**, *10*, 750.
[22] G. Zhang, H. J. Peng, C. Z. Zhao, X. Chen, L. D. Zhao, P. Li, J. Q. Huang, Q. Zhang, *Angew. Chem., Int. Ed.* **2018**, *57*, 16732.
[23] S. Li, W. Zhang, J. Zheng, M. Lv, H. Song, L. Du, *Adv. Energy Mater.* **2020**, *11*, 1606823.
[24] C. Yuan, X. Yang, P. Zeng, J. Mao, K. Dai, L. Zhang, X. Sun, *Nano Energy* **2021**, *84*, 105928.
[25] L. Ren, X. Cao, Y. Wang, M. Zhou, W. Liu, H. Xu, H. Zhou, X. Sun, *J. Alloys Compd.* **2023**, *947*, 169362.
[26] Y. Wang, L. Ren, Q. Zhang, A. H. Pato, J. Liu, X. Lu, W. Liu, *ACS Appl. Mater. Interfaces* **2024**, *16*, 47674.
[27] B. Zhong, J. Wu, L. Ren, T. Zhou, Z. Zhang, W. Liu, H. Zhou, *Energy Storage Mater.* **2022**, *50*, 792.
[28] Y. Wang, L. Ren, J. Liu, X. Lu, Q. Wang, M. Zhou, W. Liu, X. Sun, *ACS Appl. Mater. Interfaces* **2022**, *14*, 50982.
[29] N. Zhu, Y. Yang, Y. Li, Y. Bai, J. Rong, C. Wu, *Carbon Energy* **2023**, *6*, 423.
[30] T. Tao, S. Lu, Y. Fan, W. Lei, S. Huang, Y. Chen, *Adv. Mater.* **2017**, *29*, 1700542.
[31] K. Qin, K. Holguin, M. Mohammadiroudbari, J. Huang, E. Y. S. Kim, R. Hall, C. Luo, *Adv. Funct. Mater.* **2021**, *31*, 2009694.
[32] W. Lu, Z. Wang, G. Sun, S. Zhang, L. Cong, L. Lin, S. Chen, J. Liu, H. Xie, Y. Liu, *J. Energy Chem.* **2023**, *80*, 32.
[33] Z. Du, X. Chen, W. Hu, C. Chuang, S. Xie, A. Hu, W. Yan, X. Kong, X. Wu, H. Ji, L. J. Wan, *J. Am. Chem. Soc.* **2019**, *141*, 3977.
[34] J. Wang, L. Jia, J. Zhong, Q. Xiao, C. Wang, K. Zang, H. Liu, H. Zheng, J. Luo, J. Yang, H. Fan, W. Duan, Y. Wu, H. Lin, Y. Zhang, *Energy Storage Mater.* **2019**, *18*, 246.
[35] L. Ren, J. Liu, Y. Zhao, Y. Wang, X. Lu, M. Zhou, G. Zhang, W. Liu, H. Xu, X. Sun, *Adv. Funct. Mater.* **2023**, *33*, 2210509.
[36] L. Ren, K. Sun, Y. Wang, A. Kumar, J. Liu, X. Lu, Y. Zhao, Q. Zhu, W. Liu, H. Xu, X. Sun, *Adv. Mater.* **2023**, *36*, 2310547.
[37] Y. Li, H. Sun, L. Ren, K. Sun, L. Gao, X. Jin, Q. Xu, W. Liu, X. Sun, *Angew. Chem., Int. Ed.* **2024**, *63*, 202405334.
[38] R. Yan, Z. Zhao, R. Zhu, M. Wu, X. Liu, M. Adeli, B. Yin, C. Cheng, S. Li, *Angew. Chem., Int. Ed.* **2024**, *63*, 202404019.
[39] F. Cao, X. Zhang, Z. Jin, J. Zhang, Z. Tian, D. Kong, Y. Li, Y. Li, L. Zhi, *Adv. Energy Mater.* **2024**, *14*, 2303893.
[40] A. Bhargav, J. He, A. Gupta, A. Manthiram, *Joule* **2020**, *4*, 285.
[41] G. Zhang, Y. Jia, C. Zhang, X. Xiong, K. Sun, R. Chen, W. Chen, Y. Kuang, L. Zheng, H. Tang, W. Liu, J. Liu, X. Sun, W.-F. Lin, H. Dai, *Energy Environ. Sci.* **2019**, *12*, 1317.
[42] Y. Jia, Y. Wang, G. Zhang, C. Zhang, K. Sun, X. Xiong, J. Liu, X. Sun, *J. Energy Chem.* **2020**, *49*, 283.
[43] X. Sun, Y. Tuo, C. Ye, C. Chen, Q. Lu, G. Li, P. Jiang, S. Chen, P. Zhu, M. Ma, J. Zhang, J. H. Bitter, D. Wang, Y. Li, *Angew. Chem., Int. Ed.* **2021**, *60*, 23614.
[44] Y. Jia, X. Xiong, D. Wang, X. Duan, K. Sun, Y. Li, L. Zheng, W. Lin, M. Dong, G. Zhang, W. Liu, X. Sun, *Nanomicro Lett.* **2020**, *12*, 116.
[45] W. G. Lim, C. Y. Park, H. Jung, S. Kim, S. H. Kang, Y. G. Lee, Y. C. Jeong, S. B. Yang, K. Sohn, J. W. Han, J. Lee, *Adv. Mater.* **2023**, *35*, 2208999.
[46] F. Y. Fan, W. C. Carter, Y. M. Chiang, *Adv. Mater.* **2015**, *27*, 5203.
[47] Q. Pang, D. Kundu, M. Cuisinier, L. F. Nazar, *Nat. Commun.* **2014**, *5*, 4759.
[48] G. Zhou, S. Zhao, T. Wang, S. Z. Yang, B. Johannessen, H. Chen, C. Liu, Y. Ye, Y. Wu, Y. Peng, C. Liu, S. P. Jiang, Q. Zhang, Y. Cui, *Nano Lett.* **2020**, *20*, 1252.
[49] X. Han, Z. Zhang, X. Xu, *J. Mater. Chem. A.* **2021**, *9*, 12225.

